Nanosized iron and iron–cobalt spinel oxides as catalysts for methanol decomposition

E. Manova [a,*], T. Tsoncheva [b], Cl. Estournès [c], D. Paneva [a], K. Tenchev [a], I. Mitov [a], L. Petrov [a]

[a] *Institute of Catalysis, Bulgarian Academy of Sciences, Acad. G. Bonchev Str., bl. 11, 1113 Sofia, Bulgaria*
[b] *Institute of Organic Chemistry, Bulgarian Academy of Sciences, Acad. G. Bonchev Str., bl. 9, 1113 Sofia, Bulgaria*
[c] *PNF2 – CIRIMAT, UMR 5085 CNRS/UPS/INP, Université Paul Sabatier, 118 route, de Narbonne, 31062 Toulouse Cedex 04, France*

Abstract

Nanosized iron and mixed iron–cobalt oxides supported on activated carbon materials and their bulk analogues prepared by thermal synthesis are studied by X-rays diffraction, Mössbauer spectroscopy, magnetic measurements and temperature programmed reduction. Their catalytic behavior in methanol decomposition to H_2, CO and methane is tested. Phase transformations in the metal oxides affected by the reaction medium are also investigated. Changes in the reaction mechanism of the methanol decomposition after the metal oxides deposition on the support as compared to the bulk phases are discussed.

Keywords: Nanoparticles; Iron and/or cobalt oxide catalysts; Mössbauer spectroscopy; Methanol decomposition; Magnetism

1. Introduction

Nanosized spinel ferrite particles have attracted in the past considerable attention and research efforts. Because of their technological importance in microwave industries, high-speed digital tape or disk recording, magnetic refrigeration systems and ferrofluids they are still objects of intensive investigations [1–4]. It is well established that various binary and ternary spinel ferrites are effective catalysts for a number of industrial processes such as oxidative dehydration of hydrocarbons, decomposition of alcohols, alkylation reaction, hydrodesulfurization of crude petroleum, Fischer-Tropsch reaction etc. [5–20]. Binary oxide 2–3 spinels may be described by the general formula $Me^{2+}Me_2{}^{3+}O_4$. The cation distribution in these spinels can be: (i) ''normal'', i.e. the divalent metal ions are located on the tetrahedral (A)-sites—$(Me^{2+})_A[Me_2{}^{3+}]_BO_4$; (ii) ''inverse'', i.e. the divalent metal ions occupy octahedral [B]-sites—$(Me^{3+})_A[Me^{2+}Me^{3+}]_BO_4$ and (iii) ''intermediate'' (partially inverse) between normal and inverse—$(Me_x{}^{2+}Me_\lambda{}^{3+})_A[Me_{1-x}{}^{2+}Me_{2-\lambda}{}^{3+}]_BO_4$. For spinels, where only divalent and trivalent cations are present, the inversion degree (λ) is defined as a fraction of (A)-sites occupied by trivalent ions [21]. It was also reported that, in the case of ferrites, Fe^{3+} ions could be easily shifted either to octahedral or to tetrahedral sites by varying stoichiometric ratio with the other cations. As a result, the physical and catalytic properties of the spinel oxides might be influenced not only by the nature and the oxidative state of the transition metal ions, but also by their distribution in the spinel structure [21–25]. In this aspect, the determination of cation distribution in the spinels gains a considerable interest because of its influence on their physical and chemical properties.

Methanol is expected to become one of the new liquid energy carriers because it can be synthesized from biomass, coal and natural gas, all of them being more abundant resources than the crude oil. In the last two decades among the various procedures of methanol conversion (steam reforming, partial oxidation, etc.) the methanol decomposition has received growing attention as a source of hydrogen and/or synthesis gas for chemical processes or as an ecological fuel for gas turbines, vehicles and fuel cells [26–30]. Since the methanol decomposition to hydrogen and carbon monoxide is an endothermic

* Corresponding author.
E-mail address: elina@ic.bas.bg (E. Manova).

doi:10.1016/j.apcata.2005.11.005

process, it is also suitable for chemical storage of heat. However, a significant improvement of catalysts for the methanol decomposition is desired. Various metals and metal oxides are reported to be effective catalysts for this reaction [31–35]. We established that nanoparticles of iron or iron oxide supported on mesoporous molecular sieves could substantially change the reaction selectivity, at that hydrogen and methane/or carbon monoxide being the main products [36–40]. It has been shown as well that the selectivity of methanol conversion to CO and methane could be easily controlled by varying of the supported iron oxide dispersion and its transformations provoked by the reaction medium [38]. The role of the support pore architecture on the state of the supported iron species was also widely discussed. However, only a few data on the methanol decomposition using mixed iron–cobalt oxides catalysts have been published so far. In our previous study we investigated the catalytic behavior of mechanochemically synthesized nano-dimensional iron cobalt spinel oxides in methanol decomposition. A well-defined effect of the preparation conditions and the Fe/Co ratio on the reduction and catalytic properties of iron–cobalt catalysts is established [41]. However, the obtained nanoparticles usually show a strong tendency to aggregate. The latter makes it very difficult to exploit their unique physical properties. Dispersion of the nanoparticles in a matrix [42,43] as well as their deposition on various supports [44–51] are approaches to reducing their agglomeration.

The aim of the present paper is to elucidate the changes in the catalytic behavior of iron and mixed iron–cobalt oxides in methanol decomposition after their deposition on a support. For this purpose spinel ferrites with various Co/Fe ratios were supported on activated carbon and their catalytic properties were measured. Activated carbon was chosen as a support, because of its high specific surface area, well-developed pore structure and catalytic inertness [52,53]. Special attention is paid on the phase transformations during the catalytic process and their relation to the catalytic efficiency of the samples.

2. Experimental

2.1. Materials

Granulated activated carbon with a specific surface area of 545 m^2/g and pore volume of 0.55 cm^3/g was used as a support [54]. Iron–cobalt oxide/activated carbon samples with Fe/Co ratio of 2 and 0.5 (denoted as $CoFe_2$/AC and Co_2Fe/AC, respectively) were obtained by vacuum impregnation of the activated carbon (AC) with solution of $Fe(NO_3)_3{\cdot}9H_2O$ and $Co(NO_3)_2{\cdot}6H_2O$ with the desired Fe/Co ratio. Iron oxide/activated carbon sample (Fe/AC) were also prepared by vacuum impregnation of the AC with $Fe(NO_3)_3{\cdot}9H_2O$. After drying at 473 K, the obtained materials were heated in argon at 773 K for 3 h. All samples contain 10 wt.% of metal.

Thermal synthesis of the bulk ferrites with Fe/Co ratio of 2 and 0.5 (denoted as $CoFe_2$TS and Co_2FeTS, respectively) was performed in two steps: co-precipitation and subsequent annealing of the co-precipitation precursor [41]. For the co-precipitation process, 0.5 M solutions of metal salts containing Co^{2+} and Fe^{3+}, are taken in the desired Fe/Co molar ratio. The mixed cobalt and iron hydroxide carbonate precursors were formed when 1M sodium carbonate solution is added until the solution pH reach 9. The initially formed precipitate was kept under continuous stirring for 1 h at room temperature. After filtration, washing and drying at room temperature brown substances with layered structure were produced. The as-obtained precursor powders were annealed at 773 K and 573 K to obtain $CoFe_2O_4$ ($CoFe_2$TS) and Co_2FeO_4 (Co_2FeTS), respectively. Synthesis of Fe_3O_4 (sample denoted as FeTS) was carried out following the preparative procedure described in [55].

2.2. Methods for samples characterization

2.2.1. Mössbauer spectroscopy

Mössbauer measurements of nanosize cobalt ferrite particles were carried out at room temperature (RT) and liquid nitrogen temperature (LNT) with a Wissel electromechanical Mössbauer spectrometer (Wissenschaftliche Elektronik GmbH, Germany) working at a constant acceleration mode. The experimentally obtained spectra were treated using the least squares method. The parameters of hyperfine interaction such as isomer shift (IS), quadrupole splitting (QS) and effective internal magnetic field (H_{eff}) as well as the line widths (FWHM) and the relative weight (G) of the partial components of the spectra were determined.

2.2.2. X-ray diffraction

X-ray diffraction (XRD) patterns were collected using a TUR-M62 apparatus (Germany) with Co Kα radiation, equipped with a computerized HZG-4 goniometer. Spectra interpretation was carried out using the JCPDS database.

2.2.3. Magnetic measurements

Isothermal magnetizations were obtained with a Princeton Applied Research vibrating sample magnetometer Model 155 (VSM-maximum static field of ±1.8 T). The magnetic susceptibilities were recorded on a Quantum Design Supra Conducting Quantum Interference Device (SQUID) magnetometer. The operating temperature was increased from 2 to 400 K and the applied magnetic field goes up to 50 kOe.

2.2.4. Specific surface areas measurements

Specific surface areas of all studied samples have been determined by nitrogen adsorption/desorption isotherms on a Sorpty 1750 porosimeter.

2.2.5. Temperature-programmed reduction

Temperature-programmed reduction (TPR) of the samples was carried out in the measurement cell of a differential scanning calorimeter (DSC-111, SETARAM) directly connected to a gas chromatograph (GC). Measurements were made in the 300–973 K range at 10 K/min heating rate in a flow of $Ar:H_2$ = 9:1, the total flow rate being 20 ml/min. A cooling trap

between DSC and GC removes the water obtained during the reduction.

2.2.6. Catalytic activity and selectivity measurements

The catalytic activity and selectivity measurements were performed in a fixed-bed reactor. The initial reaction mixture, which consists of methanol (partial pressure of 1.57 kPa) and Ar was passing through the reactor with WHSV of 1.5 h^{-1}. The experiments were carried out in a regime of temperature programmed reaction (2 K/min) in a temperature interval of 480–750 K. The on-line gas chromatographic analysis was performed on a Porapak Q and molecular sieve columns using both thermoconductivity and flame-ionization detectors. The yields of products were estimated using carbon-based absolute calibration method. CO and methane are the only registered carbon containing products in all cases, so their distribution was presented as CO selectivity (calculated as a ratio of yields of CO and CH_4 + CO). After the catalytic test the samples were passivated using a standard procedure as follows: cooling in a flow of argon to room temperature for 1 h and after that in a flow of argon with 5% air for 1 h.

3. Results and discussion

3.1. XRD measurements

XRD patterns of the initial samples are shown in Fig. 1. For the thermally synthesized samples well defined reflexes typical of the corresponding spinel phases are registered: Fe_3O_4 $-a = b = c = 8.39$ Å (PDF 19-0629), $CoFe_2O_4$ $-a = b = c = 8.38$ Å (PDF 22-1086), Co_2FeO_4 $-a = b = c = 8.16$ Å [56]. The average particle size calculated using the Debbye-Scherrer equation is about 42 nm for FeTS, 27 nm for $CoFe_2$TS and 7 nm for Co_2FeTS. In the case of supported compounds the XRD patterns consist of reflections typical of graphite (PDF 75-2078) and low intensity lines of Fe_3O_4 in the case of Fe/AC, $CoFe_2O_4$—for $CoFe_2$/AC and CoO (PDF 43-1004), Co_2FeO_4 and Co (Fe-Co)—for Co_2Fe/AC.

3.2. Mössbauer spectroscopy measurements

Mössbauer spectroscopy was applied to obtain more information about the phase composition, cationic occupations and/or different state distribution of iron ions in the studied ferrite materials. The points in Fig. 2 represent the experimental Mössbauer results and the continuous lines through the data points correspond to least-squares fitting. The resultant Mössbauer parameters are given in Table 1. The room temperature spectrum of FeTS and $CoFe_2$TS are composed only by sextet components. The first one includes typical sextets due to Fe^{3+} and $Fe^{3+}Fe^{2+} \rightarrow Fe^{2.5+}$ ion occupation in (A) and [B] positions, respectively. According to [57] the distribution of iron cations between the two nonequivalent cation sublattices provided by the spinel structure was calculated from equation:

$$\frac{I_{(A)}}{I_{[B]}} = \frac{f_{(A)}}{f_{[B]}} \frac{\lambda}{(2-\lambda)},$$

where $I_{(A)}$ and $I_{[B]}$ are Mössbauer sublattice areas of tetrahedral and octahedral position, respectively, $f_{(A)}$ and $f_{[B]}$—recoilless fraction of position (A) and [B]. The ratio $f_{(A)}/f_{[B]} = 0.94$ for the RT Mössbauer spectrum [58] and $f_{(A)}/f_{[B]} = 1$ for the LNT one [59]. The inversion degree of Fe_3O_4, according to cation distribution $(Fe^{3+})_{tetra}[Fe^{3+}Fe^{2+}]_{octa}O_4$ is $\lambda = 1$. In the case of $CoFe_2$TS, it should be noted that acceptable data fitting could be obtained only when the [B]-site pattern is assumed to be a superposition of more than one

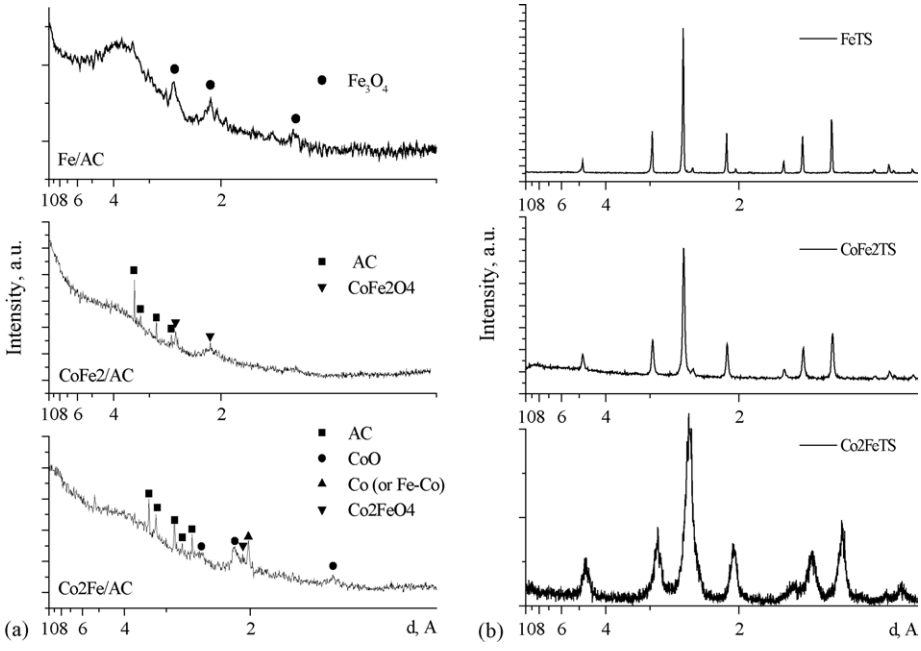

Fig. 1. XRD patterns of initial supported on AC (a) and bulk (b) iron and iron–cobalt spinel oxides.

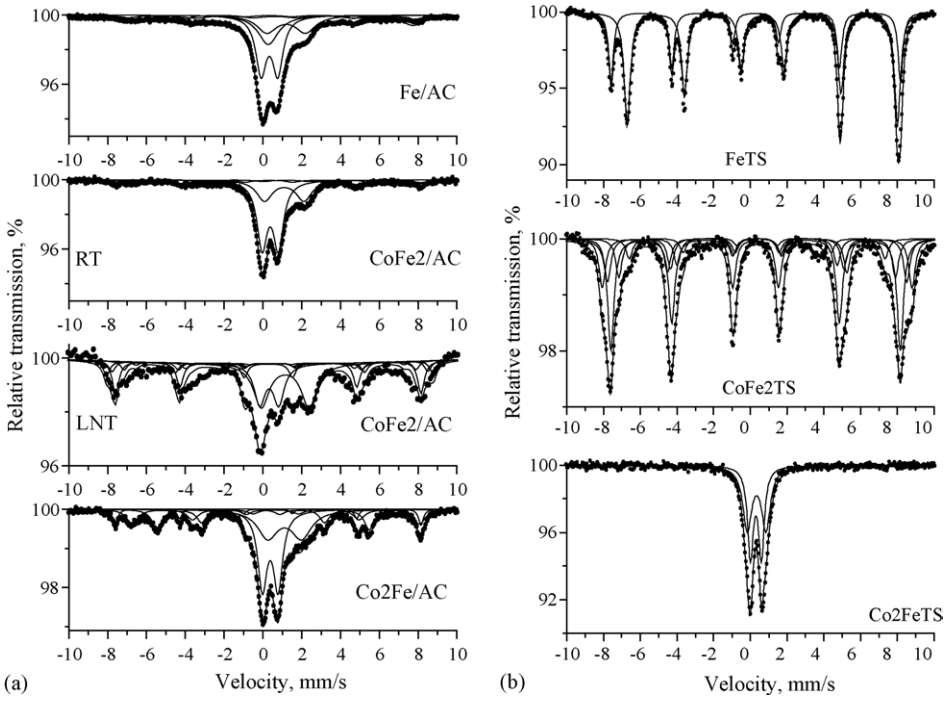

Fig. 2. Mössbauer spectra of initial supported on AC (a) and bulk (b) iron and iron–cobalt spinel oxides.

Table 1
Mössbauer parametra of initial samples

Sample	Components	IS (mm/s)	QS (mm/s)	H_{eff} (kOe)	FWHM (mm/s)	G (%)
Fe/AC	Sn–Fe^{3+}, Fe^{2+}	0.27	0.00	–	1.26	18
	Db1–Fe^{3+}	0.36	0.86	–	0.65	37
	Db2–Fe^{2+}	1.20	2.00	–	1.27	21
	Sxt1–Fe^{3+}_{tetra}	0.30	0.00	467	1.00	10
	Sxt2–$Fe^{2.5+}_{octa}$	0.60	0.00	435	1.40	14
$CoFe_2$/AC	Db1–Fe^{3+}	0.35	0.86	–	0.64	59
	Db2–Fe^{2+}	1.13	2.01	–	0.80	26
	Sxt–$Fe^{3+}_{tetra,octa}$	0.31	0.00	480	0.94	15
$CoFe_2$/AC LNT	Db1–Fe^{3+}	0.32	0.98	–	0.67	20
	Db2–Fe^{2+}	1.15	2.46	–	0.97	30
	Sxt1–Fe^{3+}_{tetra}	0.28	0.00	489	0.40	26
	Sxt2–Fe^{3+}_{octa}	0.37	0.00	524	0.40	9
	Sxt3–Fe^{3+}_{octa}	0.37	0.00	506	0.40	7
	Sxt4–Fe^{3+}_{octa}	0.37	0.00	468	0.40	6
	Sxt5–Fe^{3+}_{octa}	0.37	0.00	430	0.40	2
Co_2Fe/AC	Db1–Fe^{3+}	0.35	0.81	–	0.57	34
	Db2–Fe^{2+}	1.12	1.77	–	1.25	26
	Sxt1–Fe^{3+}_{tetra}	0.27	0.00	490	0.29	7
	Sxt2–$Fe^{2.5+}_{octa}$	0.66	0.00	460	0.69	16
	Sxt3–Fe–Co alloy	0.01	0.00	340	0.59	17
FeTS	Sxt1–Fe^{3+}_{tetra}	0.30	0.00	490	0.30	34
	Sxt2–$Fe^{2.5+}_{octa}$	0.66	0.00	457	0.60	66
$CoFe_2$TS	Sxt1–Fe^{3+}_{tetra}	0.28	0.00	490	0.41	44
	Sxt2–Fe^{3+}_{octa}	0.37	0.00	524	0.42	18
	Sxt3–Fe^{3+}_{octa}	0.37	0.00	507	0.42	16
	Sxt4–Fe^{3+}_{octa}	0.37	0.00	467	0.42	15
	Sxt5–Fe^{3+}_{octa}	0.37	0.00	432	0.42	8
Co_2FeTS	Db1–Fe^{3+}_{octa}	0.34	1.02	–	0.58	52
	Db2–Fe^{3+}_{tetra}	0.30	0.59	–	0.38	48

IS: isomer shift, QS: quadrupole splitting (Db) or shift (Sx), H_{eff}: effective magnetic field, G: relative weight.

sextet. In our cases the hyperfine interaction of the [B]-site could be fitted up to four overlapping six-line patterns, which agrees with the observations of other authors for ferrite samples. Sawatzky et al. [60] interpreted this phenomenon in terms of the random occupancy of the tetrahedral site by Fe^{3+} and Co^{2+}. Consequently, the statistical distribution of Co^{2+} ions on the (A)-site will result in appearance of different nearest neighbors to Fe^{3+} ions on the [B]-site. The intensities of the four different [B]-sites are proportional to the probabilities that a Fe^{3+} [B]-site ion has 6Fe, 5Fe1Co, 4Fe2Co and 3Fe3Co nearest neighbors. On the base of Mössbauer spectra the following cation distribution is calculated for $CoFe_2TS$-$(Co_{0.13}Fe_{0.87})[Co_{0.87}Fe_{1.13}]O_4$, so $\lambda = 0.87$. The RT spectrum of Co_2FeTS presents only doublets, which can arise from Fe in ultradispersed ferrite particles exhibiting superparamagnetic (SPM) behavior [61,62]. This particle size effect is in good agreement with the XRD data. The processing of this spectrum using two doublets model shows cation distribution of $\lambda = 0.48$, which is close to the random one and is in accordance with the results obtained by Ferreira et al. [21].

In contrast to bulk materials, Mössbauer spectra of the corresponding supported materials are more complicated and consist of sextets, doublets and singlet components. For Fe/AC they can be associated with the presence of highly dispersed ($D > 12$ nm) Fe_3O_4 ($G = 24\%$), Fe^{2+} ions in clusters (Db2, $G = 21\%$), superparamagnetic (SPM) ultradispersed ($D < 12$ nm) α-Fe_2O_3 (Db1, $G = 37\%$) and SPM Fe_3O_4 ($G = 18\%$), respectively. For $CoFe_2$/AC a RT and LNT spectra were recorded. The RT spectrum presents a superposition of sextets ($CoFe_2O_4$, $G = 15\%$) and doublets (Fe^{2+}, $G = 26\%$ and SPM $CoFe_2O_4$, $G = 59\%$). The superparamagnetic behavior of a part of $CoFe_2$/AC is confirmed by the LNT spectrum where the doublet component is decreased ($G = 15\%$) and the sextet component is increased ($G = 60\%$). The XRD pattern contains lines of activated carbon and the spinel phase $CoFe_2O_4$. Thus the phase composition of $CoFe_2$/AC is $CoFe_2O_4$ which consists of particles with large size distribution—20% with $D > 10$–12 nm, 40% with $4 < D < 10$ nm and 15% with $D < 4$ nm. Small-particle effects in the spectrum do not allow the inversion degree to be correctly determined. However for the sextet part $\lambda = 0.52$. In the case of Co_2Fe/AC the results of the XRD and MS show that a compound with a multiphase composition is synthesized—$Co_{3-x}Fe_xO_4$, $Co_xFe_{1-x}O$, Fe_3O_4 and Fe–Co alloy. In all supported compounds the presence of Fe^{2+} ions in clusters are registered which is an evidence for the interaction between the carrier and supported spinel oxide phases.

3.3. Magnetic measurements

The isothermal magnetizations of the supported phases are shown in Fig. 3. The magnetizations of all samples are weak (several emu/g), being in agreement with the amount of metal supported on these phases. The absence of saturation in the magnetic field range explored, the ''S'' shape of the curves together with the lack of coercivity indicate the presence of small magnetic particles exhibiting superparamagnetic behaviors [63,64]. A closer look to the isothermal magnetization

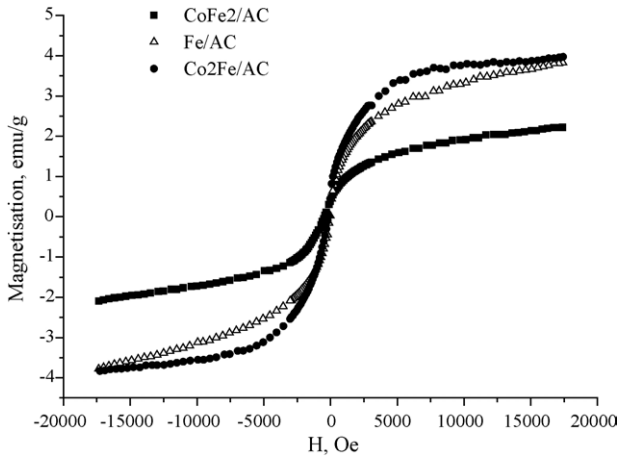

Fig. 3. Isothermal magnetizations of the supported phases.

measured up to 5 Teslas (Fig. 4) reveal the presence of small coercivity for both cobalt-spinels indicating the presence of particles exhibiting ferrimagnetic behavior at room temperature [65–69]. This is confirmed by the ZFC-FC measurement reported in Fig. 4, where no maxima are observed on the ZFC part of the curves for the Co_2Fe/AC sample and to the fact that ZFC-FC curves are never superimposed. This confirms the fact that the particles formed are size distributed and that the smaller ones exhibit superparamagnetic behavior at room temperature, whereas the bigger ones are ferrimagnets. This has already been suggested by the coexistence of doublet and sextets on the RT Mössbauer spectra. The case of the $CoFe_2$/AC sample is different as a first maximum on the ZFC curve is observed at about 260 K and a second one—above 400 K. The maximum (or drop in magnetization) on the ZFC curve observed around 260 K for the sample $CoFe_2$/AC cannot be attributed to the presence of α-Fe_2O_3. This statement is based taking into accout two conciderations: (i) Hematite exhibits a magnetic transition called Morin transition at 260 K [70]. Morin transition is a result of the action of moments of the two sublattices within the rhombohedral cell changing from parallel to the [1 1 1] direction at high temperature to perpendicular at low temperature and is accompanied by a lowering of the magnetization [71]. (ii) The opposite accident (phenomenon) should be also observed on the FC curve. Therefore, one can obviously associate these two maxima in the ZFC curve with two different magnetic phases or more probably with two populations of particles as suggested by Mössbauer spectroscopy.

3.4. TPR measurements

In Fig. 5 TPR profiles for bulk and supported iron spinel materials are presented. The reduction of the largest amount of Fe_3O_4 and Fe/AC take place in the temperature interval of 700–950 K. Two overlapping peaks with maximum at 850 and 900 K are observed, which could be associated with reduction of iron oxides. A well-defined shift of the reduction curves to the lower temperatures is found for bulk cobalt and iron binary

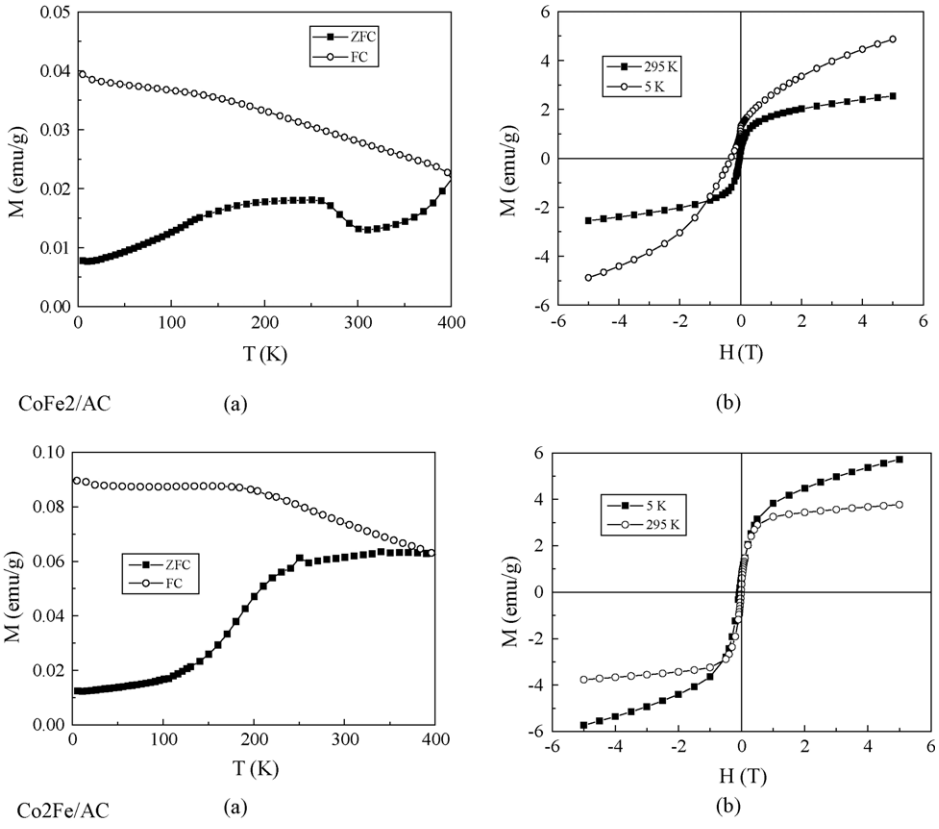

Fig. 4. Isothermal magnetization (b) and ZFC-FC measurements (a) of $CoFe_2$/AC and Co_2Fe/AC.

spinels as compared to the iron mono-component ones. Single main reduction peaks with maxima at 675 K (Co_2FeTS) and 730 K ($CoFe_2TS$) are recorded, although minor reduction shoulders appear at temperatures of 480–600 K. It is well known that the reduction of Co_3O_4 takes place in two steps—reduction of Co^{3+} to Co^{2+} in the temperature interval 550–600 K and of Co^{2+} to Co^0 in the interval of 600–700 K. It has been previously reported that reduction of two metals supported on the same support takes place simultaneously, despite of the fact that they are reduced at different temperatures when are present alone [72]. In our case, it can be tentatively assumed that hydrogen is dissociatively adsorbed on reduced Co particles, followed by spillover of hydrogen atoms, thus lowering the reduction temperature of nearby iron oxide

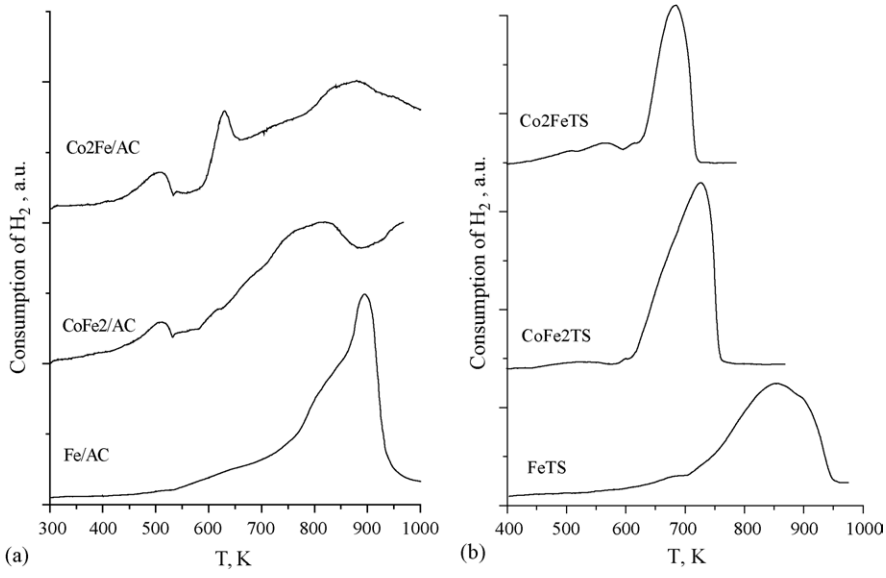

Fig. 5. TPR profiles for supported (a) and bulk (b) iron and iron–cobalt spinel materials.

Table 2
Specific surface of the supported compounds before and after catalytic test

Sample	Fe/AC initial	Fe/AC After cat. test	$CoFe_2$/AC initial	$CoFe_2$/AC after cat. test	Co_2Fe/AC initial	Co_2Fe/AC after cat. test
Surface (m^2/g)	648	692	623	538	645	500

particles. The shift of the reduction curve of $CoFe_2$TS to the higher temperature in comparison with Co_2FeTS can be ascribed to an increase in the crystallite size and to lower Co content. The TPR profile of the supported materials is totally different from that of the bulk one. The peaks of the supported materials are much broader and confirm the existence of wide particle size distribution. In the case of Co_2Fe/AC the TPR curve is composed from three peaks at 505 K, 630 K (Co^{2+}) and 860 K (Fe^{3+}), respectively, suggesting a multiphase compound, a result in accordance with data from XRD and MS.

3.5. Specific surface area measurements

The specific surface area of the supported samples before and after catalytic tests is presented in Table 2. In opposite to the iron-supported phase, the bimetallic phases show a decrease in the specific surface as a result of the catalytic test. The increase in specific surface of Fe/AC can be explained with its partial reduction, at that its chemical oxide nature being preserved or by the formation of additional amorphous carbon during the reactivity test. The decrease in the specific surface is probably related to the partial metallization observed with binary iron–cobalt supported catalysts.

3.6. Catalytic activity and selectivity measurements

In Figs. 6 and 7 the data about the methanol decomposition and product distribution (presented as CO selectivity) for various bulk and supported spinel materials are presented. Almost similar and significant methanol conversion with CO being the main carbon-containing product is registered for both bulk binary spinels just above 520–580 K (Figs. 6a and 7a). A well-defined shift of the conversion curve for FeTS to the higher temperatures is observed (Fig. 6a) and it is an indication for its lower catalytic activity in comparison with the cobalt ferrites. A low selectivity towards CO (up to 20%) is also found for this sample (Fig. 7a). The supported iron spinels exhibit catalytic activity just above 620 K (Fig. 6b). In contrast to the corresponding bulk materials, the supported samples are characterized with a similar catalytic activity despite of the differences in their composition (Fig. 6b). CO and methane in different ratio are observed in all cases and the ability of the samples to produce CO follows the order: Fe/AC $\ll$ Fe_2Co/AC $<$ $FeCo_2$/AC (Fig. 7b).

3.7. Samples characterization after catalytic test

XRD measurements of the bulk cobalt spinels used in the catalytic test reveal well defined lines of Fe_3Co_7 alloy $a = b = c = 0.284$ nm (PDF 48-1818) for Co_2FeTS and Fe_7Co_3 $a = b = c = 0.286$ nm (PDF 48-1817) for $CoFe_2$TS (Fig. 8b). No changes of the phase composition of FeTS are observed after the catalytic test. The sample exhibits a single phase—Fe_3O_4, $a = b = c = 0.839$ nm (PDF 19-629). The supported catalysts show a reduced degree of crystallinity after the catalytic test, which make more difficult the phase identification. Only the most intense lines of Fe_3O_4 (Fe/AC), $CoFe_2O_4$, α-Fe, FeC_3 (Fe_2Co/AC) and Co_2FeO_4, α-Fe (Co_2Fe/AC) appear in the spectra.

Additional information has been obtained using MS (Fig. 9, Table 3). The formation of FeCo alloy in the used bulk samples is confirmed by the Mössbauer spectra (Table 3, Fig. 9), but the appearance of Fe_3C is also registered for $CoFe_2$TS (Table 3). The sample Fe/AC exhibits lines belonging to the phases of the initial composition. The doublet of the SPM $CoFe_2O_4$ decreases due to partial transformation to cementite Fe_3C ($G = 4\%$) and FeCo alloy ($G = 7\%$), which are newly recorded phases in $CoFe_2$/AC. The disappearance of the magnetite of Co_2Fe/AC (sextet components) is observed and it is transformed into (Fe^{2+}) doublet and Fe–Co alloy sextet.

3.8. Discussion

So, the incorporation of cobalt ions within the spinel Fe_3O_4 and formation of binary metal ferrites significantly affects the

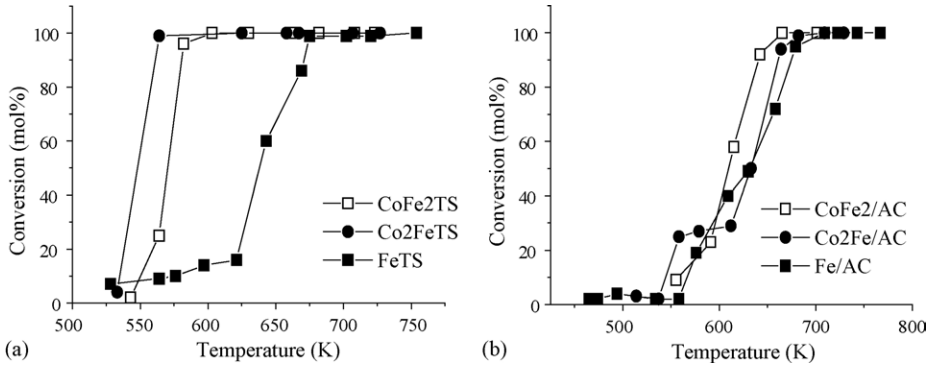

Fig. 6. Methanol conversion for bulk (a) and supported on activated carbon (b) spinel materials.

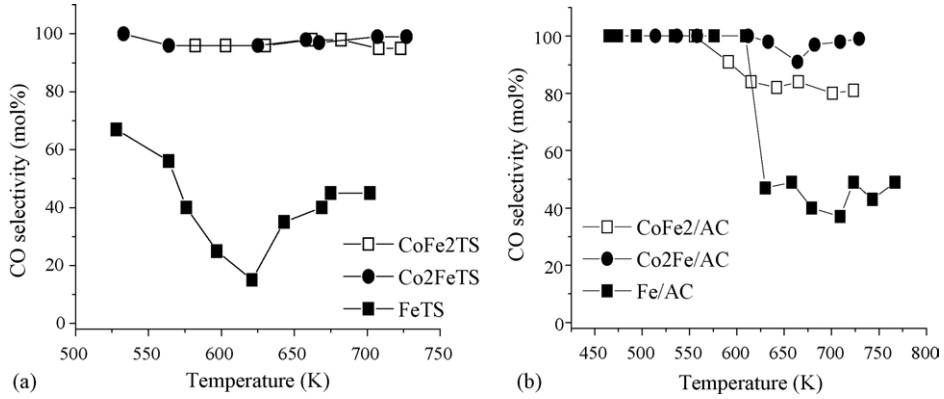

Fig. 7. CO selectivity for bulk (a) and supported on activated carbon (b) spinel materials.

reductive and catalytic properties of the samples as well as their phase transformations by the reaction medium. As a whole all binary oxides are reduced at lower temperatures as compared to the corresponding Fe_3O_4 sample (Fig. 5). A well-defined tendency to increased catalytic activity and CO selectivity is also found for the cobalt containing spinels as compared to the monocomponent ones. Significant reductive changes with the binary spinels caused due to interaction with the reaction medium are also registered. The appearance of new phases, such as CoFe alloys, metallic iron or Fe_3C is found after the catalytic test in all samples. A number of papers deal with the effect of morphological and structural peculiarities of the binary ferrites on their catalytic behavior in various processes. It was reported that they essentially depend on the distribution of the metal ions between the octahedral and tetrahedral sites of the spinel structure [12,17,21–24]. It was also established that the octahedral sites are almost exclusively exposed on the surface of the spinel crystallites and thus, the catalytic activity depends mainly on the octahedrally located cations. In this aspect the observed changes in the reductive and catalytic properties of the binary materials could be ascribed to the incorporation of Co cations into the octahedral positions of the spinel structure. Tseung et al. [73] determine the structure of Co_2FeO_4 as fully normal, which means that the second cobalt occupies tetrahedral positions. Having in mind that tetrahedral positions exhibit no catalytic activity it should be assumed that the catalytic activity of Co_2FeTS and $CoFe_2TS$ should be identical. However, the observed catalytic properties as well as the degree of inversion of the spinel rich in cobalt, determined in the present study reveal that part of cobalt ions have turned from tetrahedral to octahedral positions. This could be an explanation to the observed higher activity of Co_2FeTS as compared to $CoFe_2TS$.

However, the observed effects are less pronounced after ferrite deposition on the activated carbon. Here, mono- and bi-component iron spinels exhibit close catalytic activity (Fig. 6b). More over, both bi-component materials are almost similar not only in their catalytic activity, but in their selectivity to CO

Table 3
Mössbauer parametra of samples after catalytic test

Sample	Components	IS (mm/s)	QS (mm/s)	H_{eff} (kOe)	FWHM (mm/s)	G (%)
Fe/AC	Sn–Fe^{3+},Fe^{2+}	0.28	–	–	0.84	11
	Db1–Fe^{3+}	0.34	0.83	–	0.65	37
	Db2–Fe^{2+}	1.19	1.90	–	1.40	24
	Sxt1–Fe^{3+}_{tetra}	0.37	0.00	479	1.50	12
	Sxt2–$Fe^{2.5+}_{octa}$	0.65	0.00	451	2.00	16
$CoFe_2$/AC	Db1–Fe^{3+}	0.39	0.82	–	0.62	48
	Db2–Fe^{2+}	1.09	1.96	–	0.93	26
	Sxt1–Fe^{3+}_{tetra}	0.30	0.00	485	0.82	6
	Sxt2–$Fe^{2.5+}_{octa}$	0.60	0.00	451	1.10	4
	Sxt3–Fe^0	0.00	0.00	334	1.30	9
	Sxt4–Fe_3C	0.24	0.06	208	0.53	7
Co_2Fe/AC	Db1–Fe^{3+}	0.37	0.79	–	0.40	32
	Db2–Fe^{2+}	1.08	1.70	–	0.62	43
	Sxt–Fe–Co alloy	0.03	0.02	338	1.27	25
FeTS	Sxt1–Fe^{3+}_{tetra}	0.31	0.00	488	0.40	34
	Sxt2–$Fe^{2.5+}_{octa}$	0.67	0.00	454	0.70	66
$CoFe_2TS$	Sxt1–Fe–Co alloy	0.03	0.00	361	0.50	88
	Sxt2–Fe_3C	0.25	0.10	207	0.60	12
Co_2FeTS	Sxt–Fe–Co alloy	0.02	0.00	339	0.35	100

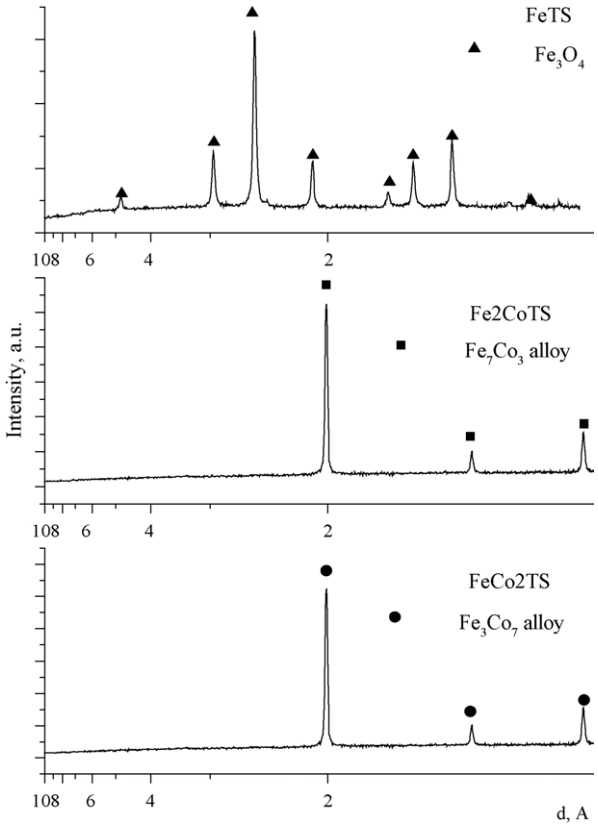

Fig. 8. XRD patterns of bulk iron and iron–cobalt spinel oxides after catalytic test.

despite the different content of cobalt in them (Fig. 7b). It is worth noting also, that the SPM part of mixed ferrites is preserved after the catalytic test (Table 3). According to our opinion different behavior of bulk and supported catalysts with respect to their spectra and catalytic properties is due to a particle size effect [74]. The bulk catalysts are built of crystallites of high degree of crystallinity and low content of structural defects. On the contrary, the supported catalysts exhibit low degree of crystallinity, the particles are ultra dispersive and correspondingly with higher degree of structural defects typical of particles with superparamagnetic behavior. In addition, the results of magnetic measurements and Mössbauer spectra reveal a wide particles size distribution at room temperature. In the course of reduction and catalytic test the support protects the oxide character of the catalysts by pores screening effect and strong interaction between the nanosized particles and the support. The smaller difference between the catalytic activity of all supported samples and especially between both binary oxides compared to the corresponding non-supported ones could be due to different ions distribution in the spinel structure after their deposition on the activated carbon. For the latter materials, the presence of cobalt ions, mainly in tetrahedral position (which as mentioned above are not responsible for the catalytic activity) could be assumed and this supposition is also confirmed by the low value of the inversion degree obtained in this case.

The study demonstrates as well the relation between catalytic activity in the reaction of methanol decomposition and the chemical composition of the catalysts. The CO selectivity increases with the cobalt incorporation in the spinel structure and it could be ascribed to the changes in the reaction mechanism of methanol decomposition. In accordance with previous investigations this follows from the noticeable difference in chemical structures of adsorbed intermediates formed on interaction of methanol with ions on the catalyst surface [75]. Methoxy intermediates, which decompose to carbon monoxide and hydrogen [76,77] could be formed on the metal and carbides surface. On contrary, the decomposition of methanol on iron oxide catalyst runs preferably to methane, the latter supposing the formation of methyl containing intermediates [78,79]. The direction of the process of hydroxyl –O–H or the –C–H carbon–hydrogen bond cleavage in methanol obviously depends on donor-acceptor properties of the catalyst

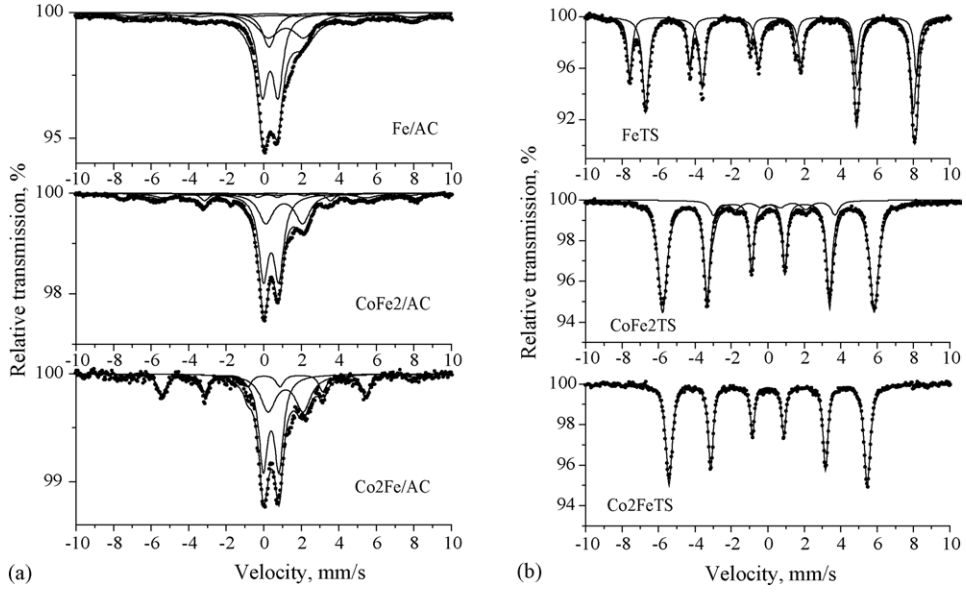

Fig. 9. Mössbauer spectra of bulk (b) and supported on AC (a) iron and iron–cobalt spinel oxides after catalytic test.

surface, i.e. on its chemical nature and electronic properties (Fermi level) which could be readily changed after the second iron incorporation into the spinel structures or after their deposition on the support.

4. Conclusion

Nanosized iron and iron–cobalt oxide particles supported on activated carbon and their bulk analogues are synthesized. The iron oxide particles are predominantly X-ray amorphous and ultradisperse. All investigated compounds possess catalytic activity in the reaction of methanol decomposition. The different catalytic behavior of bulk and supported materials is probably due to a size effect. There is significant difference in the selectivity of all catalysts in methanol decomposition to CO and methane. In the presence of Co the main carbon containing product is CO, which suppose a different reaction mechanism.

Acknowledgment

The authors thank the National Science Fund of the Bulgarian Ministry of Education and Science for the financial support of project X-1504/05.

References

[1] A. Goldman, Modern Ferrite Technology, Van Nostrand Reinhold, New York, 1990.
[2] B.M. Berkovsky, V.F. Medvedev, M.S. Krakov, Magnetic Fluids: Engineering Applications, Oxford University Press, Oxford, 1993.
[3] L. Gunther, Phys. World 3 (1990) 28–34.
[4] R.D. McMichael, R.D. Shull, L.J. Swartzendruber, L.H. Bennett, R.E. Watson, J. Magn. Magn. Mater. 111 (1992) 29–33.
[5] T. Mathew, S. Malwadkar, Shivanand Pai, N. Sharanappa, C.P. Sebastian, C.V.V. Satyanarayana, V.V. Bokade, Catal. Lett. 91 (2003) 217–224.
[6] H.H. Kung, B. Kundalkar, M.C. Kung, W.H. Cheng, J. Phys. Chem. 84 (1980) 382–388.
[7] R.J. Rennard, W.L. Kehl, J. Catal. 21 (1971) 282–293.
[8] K. Balasubramanian, V. Krishnasami, Indian J. Chem. 21A (1982) 813–815.
[9] W.S. Chen, M.D. Lee, J.F. Lee, Appl. Catal. 83 (1992) 201–211.
[10] Ch.-R. Xiong, Q.-L. Chen, W.-R. Lu, H.-X. Gao, W.-K. Lu, Z. Gao, Catal. Lett. 69 (2001) 231–236.
[11] K. Sreekumar, T. Mathew, R. Rajgopal, R. Vetrivel, B.S. Rao, Catal. Lett. 65 (2000) 99–105.
[12] K. Lazar, T. Mathew, Z. Koppany, J. Megyeri, V. Samuel, S.P. Mirajkar, B.S. Rao, L. Guczi, Phys. Chem. Chem. Phys. 4 (2002) 3530–3536.
[13] H. Grabowska, W. Kaczmarczyk, J. Wrzyszcz, Appl. Catal. 47 (1989) 351–355.
[14] S. Ghorpade, v.S. Darshane, S.G. Dixit, Appl. Catal. A 166 (1998) 135–142.
[15] S.H. Oh, R.M. Sinkevich, J. Catal. 142 (1993) 254–262.
[16] H.H. Kung, M.C. Kung, Adv. Catal. 33 (1985) 159–198.
[17] T. Mathew, S. Shylesh, S.N. Reddy, C.P. Sebastian, S.K. Date, B.S. Rao, S.D. Kulkarni, Catal. Lett. 93 (2004) 155–163.
[18] K. Sreekumar, S. Sugunan, J. Mol. Catal. A: Chem. 185 (2002) 259–268.
[19] C.G. Ramankutty, S. Sugunan, Appl. Catal. A: Gen. 218 (2001) 39–51.
[20] F. Tihay, A.C. Roger, G. Pourroy, A. Kiennemann, Energy Fuels 16 (2002) 1271–1276.
[21] T.A.S. Ferreira, J.C. Waerenborgh, M.H.R.M. Mendoca, M.R. Nunes, F.M. Costa, Solid State Sci. 5 (2003) 383–392.
[22] J.-P. Jacobs, A. Maltha, J.G.H. Reintjes, J. Drimal, V. Ponec, H.H. Brongersma, J. Catal. 147 (1994) 294–300.
[23] K.A.M. Abdel-Salaam, A.E.A.A. Said, A.M. El-Awad, E.A. Hassan, M.M.M. Abdelwahab, Collection Czech. Chem. Commun. 9 (1994) 1939–1950.
[24] J. Ziolkowski, Y. Barbaux, J. Mol. Catal. 67 (1991) 199–215.
[25] M.R. De Guire, R.C. O'Handley, G. Kalonji, J. Appl. Phys. 65 (1989) 3167–3172.
[26] L. Pettersson, K. Sjöström, Combust. Sci. Tech. 80 (1991) 265–303.
[27] J. Agrell, B. Lindstroem, L.J. Pettersson, S. Jaras, in: J.J. Spivey (Ed.), Catalysis, vol. 16, 2002, pp. 272–321.
[28] W.H. Cheng, Acc. Chem. Res. 32 (1999) 685–691.
[29] M.P. Kapoor, Y. Matsumura, J. Mol. Catal. A: Chem. 178 (2002) 169–172.
[30] R. Ubago–Perez, F. Carrasco-Marin, C. Moreno-Castilla, Appl. Catal. A: Gen. 275 (2004) 119–126.
[31] M.P. Kapoor, A. Raj, Y. Matsumura, Microporous Mesoporous Mater. 44–45 (2001) 565–572.
[32] I.A. Fisher, A.T. Bell, J. Catal. 184 (1999) 357–376.
[33] I. Matsumura, K. Tanaka, N. Tode, T. Yazawa, M. Haruta, J. Mol. Catal. A: Chem. 152 (2000) 157–165.
[34] F. Boccuzzi, A. Chiorino, M. Manzoli, J. Power Sources 118 (2003) 304–310.
[35] S.D. Jackson, D.S. Anderson, G.J. Kelly, T. Lear, D. Lennon, S.R. Watson, Top. Catal. 22 (2003) 173–182.
[36] T. Tsoncheva, M. Dimitrov, D. Paneva, I. Mitov, R. Koehn, M. Fröba, C. Minchev, Reaction Kinet. Catal. Lett. 74 (2001) 385–391.
[37] C. Minchev, R. Koehn, T. Tsoncheva, M. Dimitrov, I. Mitov, D. Paneva, H. Huwe, M. Fröba, Stud. Surf. Sci. Catal. 142B (2002) 1245–1252.
[38] R. Koehn, D. Paneva, M. Dimitrov, T. Tsoncheva, I. Mitov, C. Minchev, M. Fröba, Microporous Mesoporous Mater. 63 (2003) 125–137.
[39] C. Minchev, H. Huwe, T. Tsoncheva, D. Paneva, M. Dimitrov, I. Mitov, M. Fröba, Microporous Mesoporous Materials 81 (2005) 333–341.
[40] T. Tsoncheva, D. Paneva, I. Mitov, H. Huwe, M. Fröba, M. Dimitrov, C. Minchev, React. Kinet. Catal. Lett. 83 (2004) 299–305.
[41] E. Manova, T. Tsoncheva, D. Paneva, I. Mitov, K. Tenchev, L. Petrov, Appl. Cat. A: Gen. 277 (2004) 119–127.
[42] A. Chatterjee, D. Das, D. Chakravorty, K. Choudhury, Appl. Phys. Lett. 57 (1990) 1360–1362.
[43] X. Huang, Z. Chen, J. Magn. Magn. Mater. 280 (2004) 37–43.
[44] F. Schuth, A. Wingen, J. Sauer, Microporous Mesoporous Mater. 44 (2001) 465–476.
[45] F. Martinez, Y.-J. Han, G. Stucky, J.L. Sotelo, G. Ovejero, J.A. Metero, Stud. Surf. Sci. Catal. 142 (2002) 1109–1116.
[46] Z.Y. Yuan, W. Zhou, Z.L. Zhang, Q. Chen, B.L. Su, L.M. Peng, Stud. Surf. Sci. Catal. 141 (2002) 403–410.
[47] M. Fröba, R. Koehn, G. Bouffaund, O. Richard, G. van Tendeloo, Chem. Mater. 11 (1999) 2858–2865.
[48] T. Abe, Y. Tachibana, T. Uematsu, M. Iwamoto, J. Chem. Soc. Chem. Commun. (1995) 1617–1618.
[49] M. Iwamoto, T. Abe, Y. Tachibana, J. Mol. Catal. A 155 (2000) 143–153.
[50] W.-H. Zhang, J.-L. Shi, L.-Z. Wang, D.-S. Yan, Chem. Mater. 12 (2000) 1408–1413.
[51] A. Taguchi, F. Schueth, Microporous Mesoporous Mater. 77 (2005) 1–45.
[52] L.R. Radovic, F. Rodriguez-Reinoso, Chem. Phys. Carbon 25 (1997) 243–358.
[53] F. Rodriguez-Reinozo, Carbon 36 (1998) 159–175.
[54] D. Paneva, M. Jovanovich, T. Tsoncheva, B. Kunev, Lj. Matic, A. Terlecki-Bricevic, I. Mitov, Ch. Minchev, in: Proceedings of the 6th International Conference on Fundamental and Applied Aspects of Physical Chemistry, Belgrade Yougoslavia, 2002), pp. 186–189.
[55] U. Schwertmann, R.M. Cornell, Iron Oxide in the Laboratory: preparation and characterization, VCH, Weinheim, Basel, Cambridge, New York, 1991, pp. 111–112.
[56] P.J. Murray, J.W. Linnett, J. Phys. Chem. Solids 37 (1976) 1041–1042.
[57] V. Sepelac, D. Baabe, D. Mienert, D. Schultze, F. Krumeich, F.J. Litterst, K.D. Becker, J. Magn. Magn. Mater. 257 (2003) 377–386.
[58] E. de Grave, A. Govaert, D. Chanbaere, G. Robbrecht, Physica B 96 (1979) 103–110.
[59] G.A. Sawatzky, F. Van der Woude, A.H. Morrish, Phys. Rev. 183 (1969) 383–386.

[60] G.A. Sawatzky, F. Van der Woude, A.H. Morrish, J. Appl. Phys. 39 (1968) 1204–1206.
[61] Y. Shi, J. Ding, H. Yin, J. Alloys Comp. 308 (2000) 290–295.
[62] Y. Ahn, E.J. Choi, S. Kim, H.N. Ok, Mater. Lett. 50 (2001) 47–52.
[63] J.L. Dormann, D. Fiorani, E. Tronc, in: I. Prigogine, S.A. Rice (Eds.), Advances in Chemical Physics, 18, Wiley, 1997, pp. 283–494.
[64] C. Estournès, T. Lutz, J. Happich, T. Quaranta, P. Wissler, J.L. Guille, J. Magn. Magn. Mater. 173 (1997) 83–92.
[65] A. Hutlova, D. Nyznansky, J.L. Rehspringer, C. Estournès, M. Kurmoo, Adv. Mater. 15 (2003) 1622–1625.
[66] C. Pham-Huu, N. Keller, C. Estournès, G. Ehret, M.J. Ledoux, Chem. Comm. (2002) 1882–1883.
[67] C. Pham-Huu, N. Keller, C. Estournès, G. Ehret, M.J. Ledoux, Phys. Chem. Chem. Phys. 5 (2003) 3716–3723.
[68] N. Keller, C. Pham-Huu, T. Shiga, C. Estournès, M.J. Ledoux, J. Magn. Magn. Mater. 272–276 (2004) 1642–1644.
[69] N. Keller, C. Pham-Huu, C. Estournès, G. Ehret, M.J. Ledoux, Carbon 42 (2004) 1395–1399.
[70] F.J. Morin, Phys. Rev. 78 (1950) 819–820.
[71] C.G. Shull, W.A. Stranser, E.O. Wollan, Phys. Rev. 83 (1951) 333–345.
[72] S. Kacimi, D. Duprez, Stud. Surf. Sci. Catal. 71 (1991) 581–587.
[73] A.C.C. Tseung, J.R. Goldstein, J. Mater. Sci. 7 (1972) 1383–1390.
[74] L. Guczi, Catal. Today 101 (2005) 53–64.
[75] M. Mavrikakis, M.A. Barteau, J. Mol. Catal. A: Chem. 131 (1998) 135–147.
[76] J. Zawadzki, B. Azambre, O. Heintz, A. Krzton, J. Weber, Carbon 38 (2000) 509–515.
[77] N. Takezawa, N. Iwasa, Catal. Today 36 (1997) 45–56.
[78] R.J. Levis, J. Zhicheng, N. Winograd, J. Am. Chem. Soc. 110 (1988) 4431–4432.
[79] R.J. Levis, J. Zhicheng, N. Winograd, J. Am. Chem. Soc. 111 (1989) 4605–4612.